Chemical Science

ROYAL SOCIETY OF CHEMISTRY

EDGE ARTICLE

View Article Online
View Journal | View Issue

Cite this: *Chem. Sci.*, 2026, **17**, 6165

All publication charges for this article have been paid for by the Royal Society of Chemistry

Nanoscale Ru unlocking nanoneedles assembled into hierarchical CoO microspheres for efficient nitrate-to-ammonia electroconversion

Jinxiu Zhao, [a] Xuejing Liu,[b] Xiang Ren, *[b] Dan Zhao,[b] Zhen Li,[b] Qing Kang, [b] Chang-wen Zhang,[c] Linrui Hou, [a] Qin Wei *[b] and Changzhou Yuan *[a]

Received 26th November 2025
Accepted 20th January 2026

DOI: 10.1039/d5sc09240j

rsc.li/chemical-science

Because of the strong ability of cobalt oxide (CoO) to render active hydrogen (*H) for selective hydrogenation of NO_3^-, it is well established as a promising catalyst for the electrocatalytic reduction of NO_3^- to ammonia ($eRNO_3^-$-to-NH_3) for green NH_3 synthesis along with NO_3^- pollutant treatment. Unfortunately, its practical application is severely limited by easy agglomeration, weak NO_3^- adsorption, and the side reaction of H* coupling, causing the blockage of active sites and low selectivity of NH_3. For this, we purposefully designed a hetero hybrid electrocatalyst (denoted as CoO–Ru/CC), where nano-dimensional metallic Ru is anchored onto nanoneedles assembled into hierarchical CoO microspheres that are self-supported on carbon cloth (CC). Because of the vertical order open architecture, intrinsic oxygen vacancies, and local electric field in the self-standing CoO–Ru heterostructure, there are abundant active sites, efficient adsorption of NO_3^-, weakened N–O bonds, and a reduced reaction energy barrier, as well as high reduction selectivity. CoO–Ru/CC efficiently catalyzes $eRNO_3^-$ to NH_3 with a high NH_3 yield rate of 2.502 mg h^{-1} $cm_{cat.}^{-2}$ and faradaic efficiency of 93.41%. *In situ* characterization provided evidence for the $*NO_3$–$*NO_2$–*NO–*N–*NH–$*NH_3$ pathway involving the reaction mechanism for CoO–Ru/CC. Additionally, constructed CoO–Ru/CC-based Zn–NO_3^- batteries exhibited remarkable power density. More significantly, the in-depth insights we achieved offer meaningful guidance for rationally designing advanced CoO-based catalysts for high-efficiency $eRNO_3^-$-to-NH_3 electroconversion.

1. Introduction

Ammonia (NH_3) is an important and indispensable chemical raw material that is widely used in pharmaceuticals, nitrogen fertilizer, and in other fields.[1] What is more, thanks to the remarkable advantages of high hydrogen content, easy liquefaction, and no carbon emission, NH_3 can be used as a hydrogen storage medium or direct fuel due to its high energy density (4.3 kWh L^{-1}), which will provide an important technical method to achieve peak carbon and carbon neutrality.[2] At present, the annual production of NH_3 is approximately 160 million, and it is mainly dependent on the production mode of gray NH_3 with high energy consumption and carbon dioxide discharge tons, which is obtained *via* the Haber–Bosch process. Obviously, the gray NH_3 route contradicts the goal of carbon neutrality.[3,4] In recent years, renewable energy sources such as wind and solar power have been used to generate electricity, promoting the development of production modes for green NH_3.[5] It is crucial to search for a suitable nitrogen source as the feedstock for NH_3 synthesis. Compared to the N≡N bond energy (941 kJ mol^{-1}) of N_2,[6] the N=O bond energy (204 kJ mol^{-1}) of NO_3^- is much lower.[7] NO_3^- is widely present in agricultural and industrial wastewater, and it severely affects the environment and human health.[8] Consequently, the electroreduction of NO_3^- to NH_3 (*i.e.*, $eRNO_3^-$-to-NH_3) will open a more valuable route to generate NH_3. Although electrochemical NO_3^- reduction overcomes the barrier of reactant activation, the $eRNO_3^-$ to NH_3 process involves three deoxidation reaction steps accompanied by multiple coupled electron-proton transfer, resulting in unsatisfactory reaction kinetics and low NH_3 selectivity.

The strategies to improve $eRNO_3^-$-to-NH_3 performance include catalyst design,[9–13] electrolyte modulation,[14] and pulse electroreduction implementation.[15,16] Designing efficient catalysts has been considered as the most robust strategy, and corresponding investigations have been extensively retrieved.[17–30] For example, Ghorai and coauthors reported transition metal phthalocyanine-based systems for $eRNO_3^-$-to-NH_3 conversion.[18–20] The adsorption and hydrogenation steps of

[a]*School of Material Science & Engineering, University of Jinan, Jinan 250022, P. R. China. E-mail: mse_yuancz@ujn.edu.cn; ayuancz@163.com*

[b]*Collaborative Innovation Centre for Green Chemical Manufacturing and Accurate Detection, School of Chemistry and Chemical Engineering, University of Jinan, Jinan 250022, P. R. China. E-mail: chem_renx@163.com; sdjndxwq@163.com*

[c]*School of Physics and Technology, University of Jinan, Jinan 250022, P. R. China*

NO_3^- are important for achieving highly effective catalysis of $eRNO_3^-$ to NH_3.[31,32] Thus, the designed catalyst should exhibit appropriate adsorption strength for NO_3^-, and a series of deoxidation intermediates such as $*NO_2$ and *NO.[33,34] Furthermore, it also requires regulating the massive amount of active hydrogen (*H) generated by water (H_2O) splitting for the consumption of intermediates ($*NO_3$, $*NO_2$, *NO, and *N), rather than catalyzing further reduction to hydrogen gas (H_2).[35–38] Cobalt-based oxides, particularly CoO, can be used for $eRNO_3^-$-to-NH_3 conversion because they can produce sufficient *H from H_2O dissociation, and the Co(II) species plays a relatively pivotal role for selective hydrogenation of NO_3^-.[22–25] However, conventional CoO synthesis methods are always prone to agglomeration under high temperature, thereby resulting in a blockage of active sites. Moreover, CoO is relatively limited in terms of weak adsorption for NO_3^- due to the electron-donating properties of NO_3^- and H_2O, which reduce the performance of the NO_3^- reaction. The d-orbital energy level of Ru is comparable to the lowest unoccupied molecular π^* orbital of NO_3^-, which forms the affinity in between.[26,27] The regulation of catalyst nanomaterialization has been identified as an effective strategy to significantly increase the electrolyte/electrode contact area and the number of active sites, thereby demonstrating catalytic activity with greater efficiency. Consequently, a promising strategy is a design metal–semiconductor heterointerface consisting of a Ru and CoO nanoarray structure, in which the combined configuration would synergistically promote the electrochemically active area and affinity of CoO for NO_3^-. However, it is still an enormous challenge to maximize the advantages of CoO and Ru *via* the smart integration of the two for efficient $eRNO_3^-$-to-NH_3.

Over the past five years, zinc-nitrate ($Zn–NO_3^-$) batteries have undergone rapid development due to their high theoretical energy density of 1051 Wh kg^{-1}.[39] The aqueous $Zn–NO_3^-$ battery is also known as a clean energy battery, and it can realize NO_3^- removal and NH_3 synthesis during the discharge process. To further promote the development of the $Zn–NO_3^-$ battery, it is highly necessary to design and develop efficient electrode materials to simultaneously balance the high-power-density merit and long-duration cycling stability of the battery, as well as the efficient NH_3 synthesis.

With these comprehensive considerations in mind, we elegantly constructed a high-efficiency heterointerface catalytic platform (marked as CoO–Ru/CC), where pre-reduced nanodimensional Ru was uniformly well anchored on CoO nanoneedles (NNs) assembled into hierarchical microspheres (MSs) that were self-supported upon carbon cloth (CC), which can be used for efficiently catalyzing the reaction of $eRNO_3^-$-to-NH_3. In this heterointerface catalytic system, as authenticated by the physicochemical and theoretical characteristics, electron transfer from Ru to CoO occurs at the interface, which not only reduces the adsorption-free energy for NO_3^- species, but promotes the hydrogenation process of NO_3^- by inhibiting the coupling of *H.

Because of these appealing structural and componential merits, at −1.0 V *versus* reversible hydrogen electrode (*vs.* RHE), the NH_3 faradaic efficiency (FE_{NH_3}) reached the maximum value of 93.41% with an NH_3 yield rate (Y_{NH_3}) of 2.502 mg h^{-1} $cm_{cat.}^{-2}$. Additionally, *in situ* Raman and attenuated total reflectance Fourier transform infrared (ATR-FTIR) spectroscopy provided evidence that the key *NO and *NH intermediates were involved in the $eRNO_3^-$-to-NH_3 process, which is referred to as the $*NO_3–*NO_2–*NO–*N–*NH–*NH_2–*NH_3$ pathway. Moreover, the CoO–Ru/CC cathode-assembled $Zn–NO_3^-$ battery exhibited a power density of 7.41 mW cm^{-2} and a high FE_{NH_3} faradaic efficiency of 89.60%. Therefore, we propose a facile but efficient strategy for improving the $eRNO_3^-$-to-NH_3 conversion efficiency and constructing a high-performance $Zn–NO_3^-$ battery.

2. Experimental section

2.1. Synthesis of CoO/CC

For CoO/CC synthesis, 2 mmol of cobalt chloride hexahydrate ($CoCl\cdot 6H_2O$) and 10 mmol of urea ($CO(NH)_2$) were dissolved in 40 mL water. The homogeneous solution was transferred into a reactor with a pre-positioned carbon cloth (CC) that was pretreated by an acid washing method.[40] After holding at 120 °C for 12 h, the precursor was chemically grown upon the CC. The CoO/CC was finally obtained after calcination at 450 °C for 4 h under an Ar atmosphere.

2.2. Synthesis of Ru nanoparticles (NPs)

First, 3 mg of ruthenium(III) chloride ($RuCl_3$) was dissolved in a 20-mL mixed solution of ethanol and water with a volumetric ratio of 1 : 1. Then, 0.1 mol L^{-1} of sodium borohydride solution ($NaBH_4$) was dripped into the above solution while it was rapidly being stirring. Accordingly, the Ru NPs were synthesized.

2.3. Synthesis of CoO–Ru/CC

The as-obtained CoO/CC was completely immersed in the solution containing Ru NPs for 2 h. After solidification at 400 °C for 30 min under an Ar atmosphere, the Ru–CoO/CC hybrid electrocatalyst was obtained.

2.4. Material characterization

The powder X-ray diffraction (XRD) data and X-ray photoelectron spectroscopy (XPS) spectra were obtained through use of a SmartLab SE XRD power instrument (Rigaku, Japan) and Axis Supra X-ray photoelectron spectrometer (Shimadzu, Japan), respectively. The morphology images were acquired from field emission scanning electron microscopy (FESEM, Gemini 300, Zeiss, Germany) and transmission electron microscopy (TEM) (JEM-2100, Zeiss, Germany). Elemental species and distribution were obtained by energy-dispersive X-ray spectroscopy (EDS) (X-Max^N 50, Oxford, China). The concentration of products was measured using a UV-vis spectrophotometer (UV-2700, Shimadzu, Japan). ^{1}H nuclear magnetic resonance (^{1}H-NMR) spectra were tested from an AVANCE III HD 600 MHz NMR spectrometer (Bruker, Germany). Raman measurements were carried out with an in *Via* Reflex (Renishaw, England). Attenuated total reflectance Fourier transform infrared (ATR-FTIR)

spectroscopy was performed using a Nicolet 8700 spectrometer (Thermo Fisher, U.S.A.) with a mercury cadmium telluride (MCT) detector.

2.5. Electrochemical measurements

To evaluate the NO_3^- reduction reaction performance of the prepared catalysts, an H-type electrolytic cell was assembled with a standard three-electrode system, in which CoO–Ru/CC or CoO/CC, Pt wire, and Ag/AgCl were used as the working electrode (0.5 × 0.5 cm^2), counter electrode, and reference electrode, respectively. The $Na_2SO_4/NaNO_3$ or Na_2SO_4 electrolyte in an H-type electrolytic cell was isolated by a proton exchange membrane (PEM). Experiments were conducted at 25 °C. Unless noted, all potentials used the reversible hydrogen electrode (RHE) scale. The conversion equation is as follows:

$$E(vs.\ \mathrm{RHE}) = E(vs.\ \mathrm{Ag/AgCl}) + 0.197 + 0.059 \times \mathrm{pH} \quad (1)$$

2.6. Determination of NH_3

The produced NH_3 was estimated by the indophenol blue spectrophotometric method.[41] Herein, the linear equation of the standard curve was obtained ($y = 0.4891x + 0.02329$, $R^2 = 0.9974$).

The Y_{NH_3} and FE_{NH_3} were calculated using the following equations:

$$Y_{NH_3} = \frac{1000 \times c_{NH_3} \times V}{17 \times t \times A} \quad (2)$$

$$FE_{NH_3} = \frac{8 \times F \times c_{NH_3} \times V}{17 \times 10^6 \times Q} \times 100\% \quad (3)$$

where c_{NH_3} (mg L^{-1}), V (L), t (h), A (cm^2), F, and Q (C) denote the measured NH_3 electrolyte volume, reaction time, the geometric area of the catalyst, Faraday constant (96485 C mol^{-1}), and quantity of electric charge, respectively.

2.7. Electrochemically active surface area (ECSA)

The electrochemically active surface area (ECSA) was calculated using the following equations:

$$\mathrm{ESCA} = R_f \times A \quad (4)$$

$$R_f = \frac{C_{dl}}{C_s} \quad (5)$$

where R_f, C_{dl} (μF cm^{-2}), and C_s (μF cm^{-2}) denote the roughness factor of the working electrode, the double-layer capacitance, and the specific capacitance of the smooth electrode surface, respectively.

2.8. DFT calculation details

Density functional theory (DFT) calculations were performed by the Vienna *Ab initio* Simulation Package (VASP).[42] The interactions of core-valence electrons and electron exchange-correlation energy were calculated by the projector-augmented wave (PAW) method and generalized gradient approximation with the Perdew–Burke–Ernzerhof (PBE) functional.[43,44] The DFT + Hubbard U approach with $U_{eff} = 4.1$ eV were employed to treat the strong on-site coulomb interaction of localized electrons, and the optimized lattice parameters of CoO were $a = b = c = 4.261$ Å.[45] The CoO–Ru interfacial structure was constructed by creating a 6 × 6 supercell of CoO(200) and a 7 × 7 supercell of Ru(200), and a 15-Å-thick vacuum region was employed between the adjacent slabs. The atoms in the top four layers and one layer were relaxed for the CoO(200) and Ru(200) surfaces, while other atoms were fixed. The kinetic energy cutoff was set to 400 eV. The convergence criteria of total energy and the optimized force on each atom were less than 10^{-5} eV and 0.05 eV $Å^{-1}$, respectively. The Gamma-center Brillouin zone uniform sampling method was used for DFT self-consistent computation. The VASPKIT code was used to calculate the post-processing of the VASP data.[46] The crystal structures were created by the VESTA visualization program.[46,47]

Additionally, the ΔG of each elementary step for eRNO_3^--to-NH_3 is defined as:[48]

$$\Delta G = \Delta E + \Delta \mathrm{ZPE} - T\Delta S \quad (6)$$

where ΔE, T, ΔZPE, and ΔS denote the energy change from DFT calculations, tested temperature (298.15 K), correction of zero-point energy, and entropy, respectively. The database for thermal corrections of gas molecules was used, and gaseous HNO_3 was chosen as a reference to directly avoid the calculation for the energy of charged NO_3^-.[49]

2.9. Zn–NO_3^- batteries

The cathode and anode of the Zn–NO_3^- battery were CoO–Ru/CC or CoO/CC and a Zn plate (1 × 1 cm^2), respectively. The aqueous solutions of catholyte and anolyte were 6 M KOH + 0.01 M $NaNO_3$ and 6 M KOH + 0.02 M $Zn(CH_3COO)_2$, respectively. The discharge time and mass loss of the Zn plate used for calculating the specific capacity were 337.6 h and 0.5331 g, respectively.

3. Results and discussion

3.1. Structural and physicochemical characterization

Fig. 1a schematically illustrates the fabrication process for the CoO–Ru/CC tandem catalyst. The self-standing CoO NN array-constructed MSs grow on the CC *via* the hydrothermal reaction and annealing under an argon (Ar) atmosphere. Subsequently, the Ru NPs, which are synthesized by simple chemical reduction, are adsorbed and solidified on each CoO NW building block. X-ray diffraction (XRD) technique was used to analyze the crystal information. The XRD pattern of CoO/CC (Fig. 1b) exhibits characteristic peaks at $2\theta = 36.5°$, 42.4°, and 61.5°, corresponding to the crystal faces of (111), (200), and (220) for the face-centered cubic CoO (JCPDS No. 48-1719), respectively,[50] and the reflection at $2\theta = 44.5°$ was attributed to the CC substrate. As for CoO–Ru/CC, in addition to the characteristic signals of CoO and CC, the characteristic peak of the

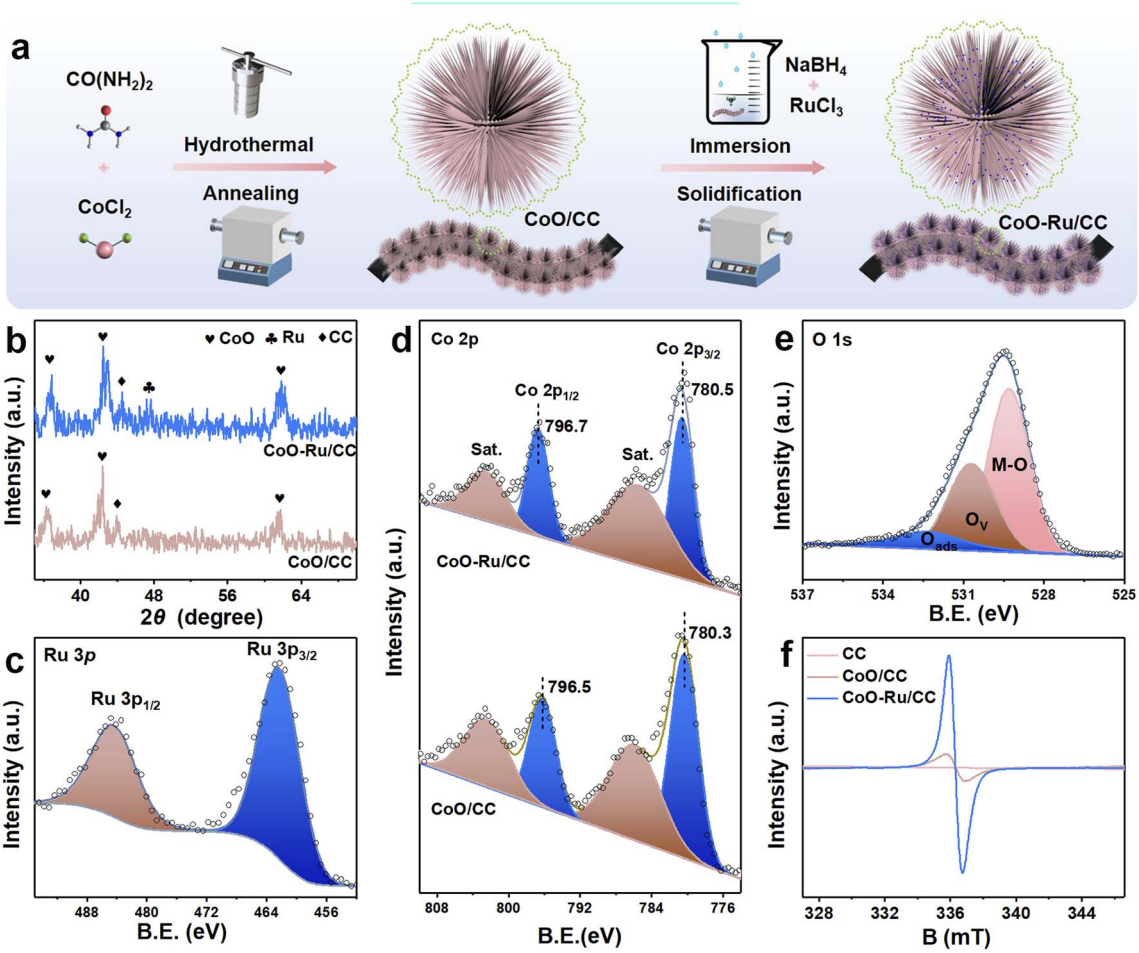

Fig. 1 (a) A schematic diagram to illustrate the fabrication process of CoO–Ru/CC. (b) XRD patterns of CoO/CC and CoO–Ru/CC. (c) The XPS spectrum of CoO–Ru/CC at the Ru 3p core level. (d) XPS spectra of CoO/CC and CoO–Ru/CC at the Co 2p core level. (e) The XPS spectrum of CoO–Ru/CC at the O 1s core level. (f) EPR spectra of CoO–Ru/CC, CoO/CC, and pure CC.

Ru (200) crystal face was observed at $2\theta = 47.4°$ (JCPDS No. 88-2333).[51]

To increase our understanding of the composition and electronic valence state, X-ray photoelectron spectroscopy (XPS) tests were conducted. Compared to the XPS survey spectrum of CoO/CC (Fig. S1, SI), except for the peaks of Co 2p, O 1s, and C 1s, CoO–Ru/CC shows characteristic peaks of Ru 3p at a binding energy (B.E.) of 462 and 484 eV, indicating the successful composite of Ru and CoO. In the fine spectra of Ru 3p (Fig. 1c), the B.E. peaks located at 462.5 eV and 484.6 eV were assigned to Ru $3p_{3/2}$ and Ru $3p_{1/2}$ of Ru^0, respectively.[52] The XPS spectra of Ru 3d and C 1s were mutually superimposed (Fig. S2), where the B.E. peaks centered at 283.8/286.3 eV and 284.8/289.2 eV correspond to Ru $3d_{5/2}$/Ru $3d_{5/2}$ of Ru^0 and the C–C/O–C=O bond, respectively.[53,54] In the Co 2p core level of CoO/CC (Fig. 1d), the doublet peaks at 780.3/796.5 eV belong to Co $2p_{3/2}$/Co $2p_{1/2}$ of divalent Co, and the other peaks are ascribed to satellite (Sat.) peaks.[55] Compared to CoO/CC, the B.E. positive shift of Co 2p in CoO–Ru/CC occurs with a gap of 0.2 eV, which should be attributed to the electron transfer between Ru and CoO after they combined.[55] The interfacial electron transfer was confirmed by ultraviolet photoelectron spectroscopy (UPS) spectra (Fig. S3). The work function (Φ) of CoO–Ru/CC (8.0 eV) is lower than that of CoO/CC (9.0 eV), indicating that electrons are transferred from Ru to CoO. The electron transfer usually plays a crucial role in improving the stability, catalytic activity, and selectivity of heterointerface catalysts.[56] Regarding the core-level O 1 s spectra (Fig. 1e), the B.E. peaks centered at 529.7, 530.7, and 531.7 eV are related to the lattice oxygen (M–O), oxygen vacancy (O_V), and adsorbed oxygen (O_{ads}) species, respectively.[57] Compared to CC, CoO–Ru/CC and CoO/CC emitted electron paramagnetic resonance (EPR) signals at $g = 2.002$, which become even more significant for the case of CoO–Ru/CC (Fig. 1f), featuring the irrecusable fact that the binding of Ru increases the concentration of O_V in the CoO sample. Over the electroreduction of NO_3^-, the introduced O_V can be filled by the O atoms in NO_3^-, weakening the N–O bond and restraining the formation of byproducts, which results in high faradaic efficiency and ammonium selectivity.[58] In addition, the O_V in CoO can strengthen metal-support interaction, limiting the agglomeration of Ru NPs.[59]

As seen from field emission scanning electron microscopy (FESEM) images of the as-synthesized CoO/CC product (Fig. 2a–c and S4), apparently, there are many sea urchin-like MSs

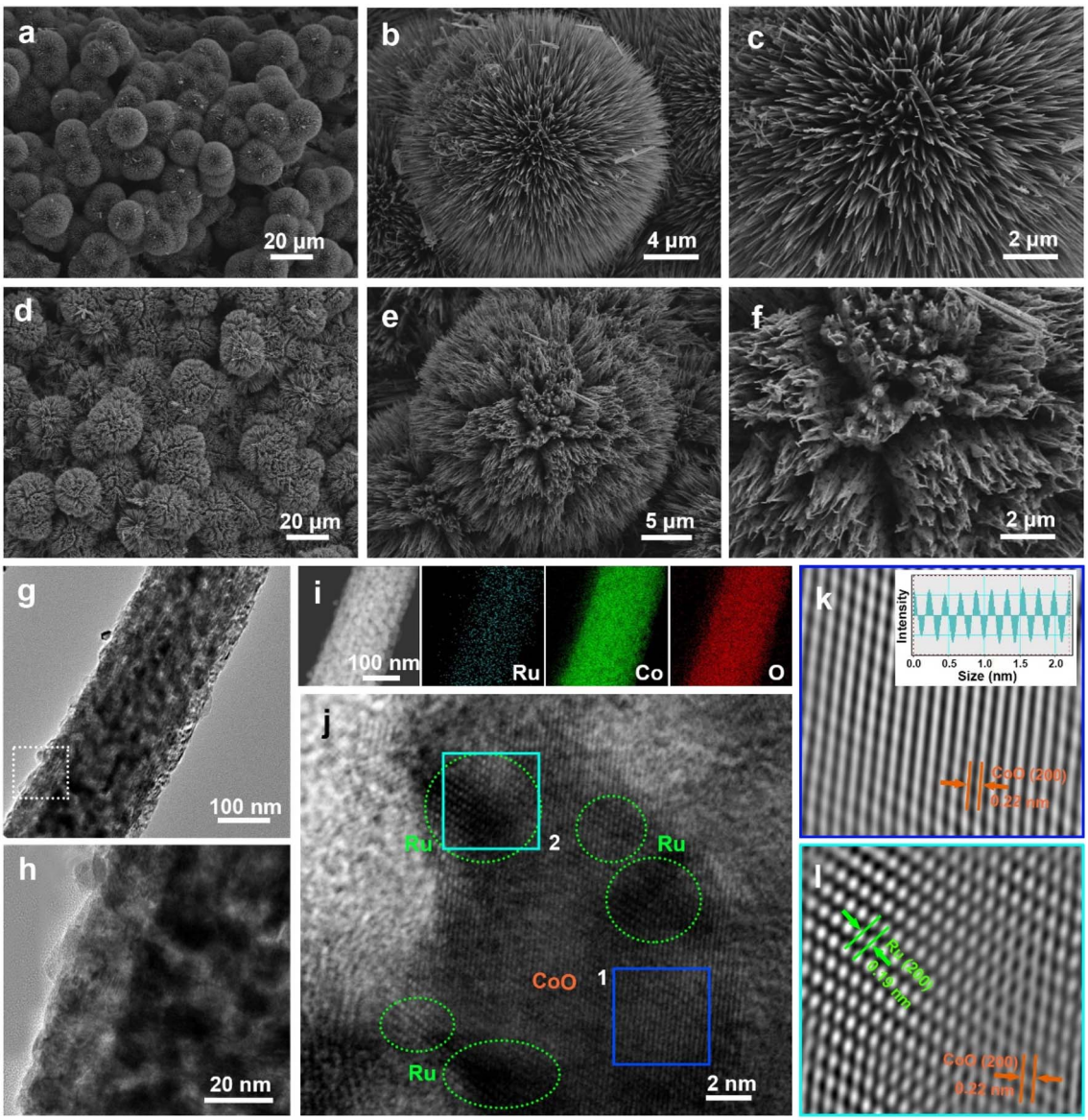

Fig. 2 FESEM images of (a–c) CoO/CC and (d–f) CoO–Ru/CC. (g, and h) TEM images, and (i) STEM and corresponding EDX element mapping images of CoO–Ru. (j) HRTEM and corresponding IFFT images from (k) region 1 and (l) region 2. The inset in panel k shows the intensity line profile.

(approximately 16.5 μm in diameter), which were assembled from NNs perpendicular to the center of the sphere, that are uniformly located on the surface of CC fibers. Such a unique hierarchical porous framework with abundant open channels guarantees plentiful exposed sites for binding Ru NPs. After being combined with Ru NPs, CoO–Ru/CC inherits the acanthospheric morphology of CoO/CC (Fig. 2d and S5), rendering abundant active three-phase sur-/interfaces. Compared to CoO, CoO–Ru adequately retains the needle-like tip structure, as shown in the high-magnification FESEM images (Fig. 2e and f). It is worth mentioning that such a vertical order open architecture will guarantee the physical capillary action of adsorption of aqueous electrolytes, and induce the generation of a local electric field that promotes the adsorption of reaction intermediates and reduces the reaction energy barrier.[60] Further transmission electron microscopy (TEM) examination (Fig. 2g and h) to visualize the CoO–Ru NNs ≈ 200 nm in diameter showed that they are composed of numerous NP subunits with diameters ranging from 5 to 15 nm. Corresponding scanning TEM (STEM) and elemental mapping images (Fig. 2i) visualized the co-existence and even distribution of the Co, O, and Ru species. As derived from energy dispersive X-ray (EDX) spectroscopy data (Fig. S6), the atomic ratio of Ru to Co is estimated to be approximately 1 : 2. The high-resolution TEM (HRTEM) image (Fig. 2j) provides clear evidence that the Ru NPs (the zones enclosed by the green line) tightly bind with CoO, and the well-defined lattice fringes are apparently discerned from the inverse fast Fourier transform (IFFT) images (Fig. 2k and l).

Specifically, the relatively regular lattice stripes with a crystal face spacing of 0.22 nm belong to the (200) crystal face of CoO (Fig. 2k). More particularly, it can be intuitively observed that Ru and CoO are closely bound together, and significant structural distortions appear at the junction of crystal planes (Fig. 2l). The lattice distortion engineering easily induces the formation of defects, which can optimize the intrinsic electronic structure of CoO–Ru and ultimately improve the intrinsic catalytic activity for conversion of eRNO_3^--to-NH_3.

3.2. Electrocatalytic nitrate reduction performance and mechanism analysis

The electrochemical measurement was carried out in an H-type electrocatalytic cell (Fig. S7). Linear sweep voltammetry (LSV) was used for the preliminary evaluation of the NO_3^- reduction reaction (NO_3^-RR) characteristics. Fig. 3a shows the LSV curves of the CoO–Ru/CC and CoO/CC catalysts in 0.1 M Na_2SO_4 with or without 0.01 M $NaNO_3$ electrolytes (marked as Na_2SO_4/$NaNO_3$ and Na_2SO_4, respectively). In Na_2SO_4/$NaNO_3$ electrolyte (solid), the current density (j) of CoO–Ru/CC is higher than that of CoO/CC, confirming that CoO–Ru/CC gain the upper hand for NO_3^-RR activity. The values of j are attenuated in the Na_2SO_4 electrolyte (short dot), which suggests that the contribution of the HER for total j in NO_3^-RR is very low. The effect of potential on the performance of NH_3 production was verified using 1-h constant potential testing with the range of −0.6 to −1.1 V (*vs.* RHE, Fig. S8). In the j–t curves of j as a function of time, CoO–Ru/CC exhibits a higher j than CoO/CC, which is consistent with the trend of the LSV data. The generated NH_3 and nitrite (NO_2^-) byproducts from the electrolytes were tested using the spectrophotometric method, and their concrete concentrations were calculated by the standard curve (Fig. S9, and S10).[41] The ultraviolet and visible (UV-vis) spectra of electrolytes after the 1-

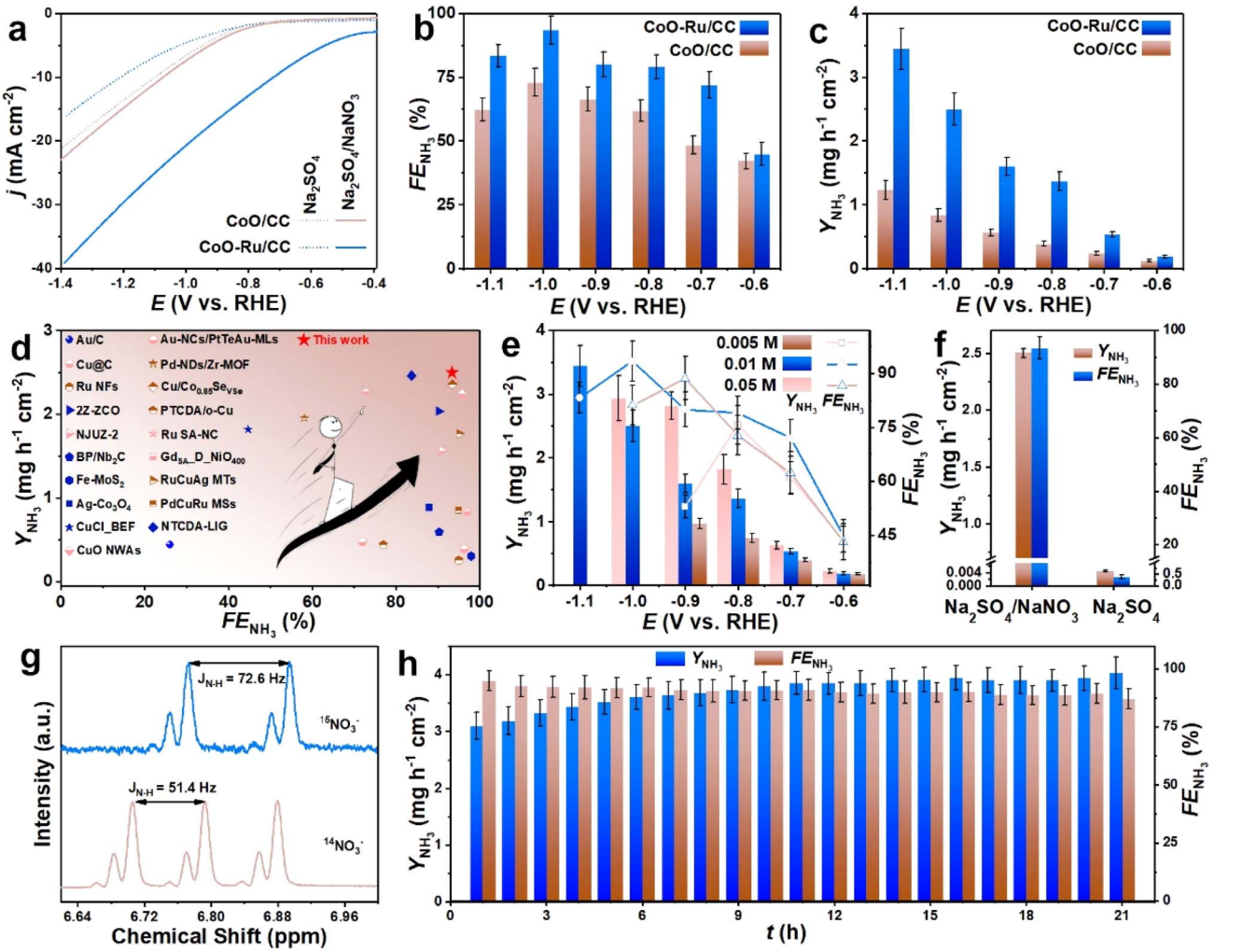

Fig. 3 (a) LSV curves of CoO–Ru/CC and CoO/CC in 0.1 M Na2SO_4 with and without 0.01 M $NaNO_3$ electrolyte. (b) $FENH_3$ and (c) YNH_3 values of CoO–Ru/CC and CoO/CC at given potentials in electrolytes with 0.01 M $NaNO_3$. (d) A comparison of Y_{NH_3} and FE_{NH_3} of CoO–Ru/CC with reported catalysts. (e) Y_{NH_3} and FE_{NH_3} of CoO–Ru/CC at given potentials in electrolytes with a series of concentrations of $NaNO_3$. (f) Y_{NH_3} and FE_{NH_3} values of CoO–Ru/CC at −1.0 V *vs.* RHE in electrolytes with and without 0.01 M $NaNO_3$. (g) ^1H NMR spectra of the electrolyte after NO_3^- reduction using $^{15}NO_3^-$ and $^{14}NO_3^-$ as the feedstock, respectively. (h) Y_{NH_3} and FE_{NH_3} values of CoO–Ru/CC in a long-term NO_3^- reduction experiment.

h electrocatalytic action of CoO–Ru/CC and CoO/CC (Fig. S11) display the positive correlation between absorbance and the provided potential. As shown in Fig. 3b, the $FENH_3$ of CoO–Ru/CC and CoO/CC presents volcanic characteristics, while the peak value (93.41%, −1.0 V *vs.* RHE) of $FENH_3$ for CoO–Ru/CC is significantly higher than that of CoO/CC (72.98%), for which the competition of the involved hydrogen evolution reaction (HER) should be responsible. Overall, at each overpotential, the Y_{NH_3} of CoO–Ru/CC is approximately 2–3 times that of CoO/CC (Fig. 3c). At the optimal potential (−1.0 V *vs.* RHE) of FE_{NH_3}, the corresponding Y_{NH_3} of CoO–Ru/CC was estimated as 2.502 mg h^{-1} $cm_{cat.}^{-2}$. The NO_2^- faradaic efficiency ($FE_{NO_2^-}$) of CoO–Ru/CC (3.10%) was lower than that of CoO/CC (12.38%), indicating that CoO–Ru/CC can suppress the generation of nitrite (Fig. S12). Significantly, the catalytic activities of CoO–Ru/CC in terms of Y_{NH_3} and FE_{NH_3} are very competitive when compared to other reported catalysts (Fig. 3d and Table S1).

To explore the effect of NO_3^- concentration on the NH_3 generation, two other concentrations (0.005 and 0.05 M) were selected for electrochemical testing. As examined from the LSV curves of CoO–Ru/CC in 0.1 M Na_2SO_4 with a series of $NaNO_3$ electrolytes (Fig. S13), clearly, the increasing trend of j is directly proportional to the concentration of NO_3^- in the electrolyte. With the NO_3^- concentration increasing from 0.005 M to 0.05 M, as evidenced from the j–t curves and corresponding UV-vis spectra (Fig. S14, and S15), j and Y_{NH_3} are positively correlated; however, the optimal FE_{NH_3} is always retained as 0.01 M (Fig. 3e). When the NO_3^- concentration reaches 0.05 M, the decrease in FE_{NH_3} is attributed to the intensification of the competitive HER.[61]

To ensure that the NH_3 product is indeed generated from the reduction of NO_3^- catalyzed by CoO–Ru/CC, a blank control experiment (Fig. S16, the electrolyte without NO_3^-) and isotope labelling test were implemented. The extremely low values of Y_{NH_3} and FE_{NH_3} confirmed that no NH_3 was produced in the blank group (Fig. 3f). In the isotope labelling experiment, an electrochemical test of NO_3^-RR was carried out in electrolytes with $^{14}NO_3^-$ or $^{15}NO_3^-$. After the electrochemical test of NO_3^-RR, the electrolyte underwent examination by ^1H nuclear magnetic resonance (^1H NMR). When the electrolyte supplies a $^{15}NO_3^-$ environment, the ^1H NMR spectrum displays a double coupling peak, and the chemical shifts are located at $\delta = 6.773$ and 6.894 ppm, respectively (Fig. 3g), rendering the coupling constant ($^1J_{N-H}$) of 72.6 Hz, which is the characteristic spectrum of $^{15}NH_4^+$. For the case of the $^{14}NO_3^-$ electrolyte, the ^1H NMR spectrum presents a triple coupling peak with chemical shifts of $\delta = 6.705$, 6.793, and 6.880 ppm, respectively, and thus, the $^1J_{N-H}$ is calculated as 51.4 Hz, corresponding to the typical split peaks of $^{14}NH_4^+$. The comparative analysis here authenticates that the produced NH_3 does come from the reduction of NO_3^-.

The durability of the CoO–Ru/CC catalyst, which is of great importance in promoting industrial applications, was evaluated *via* long-time chronoamperometric measurement. In the electrolytes of 0.1 M Na_2SO_4 and 0.05 M $NaNO_3$, the j–t curves of CoO–Ru/CC exhibit stability for at least 21 h at a potential of −1.0 V (*vs.* RHE) (Fig. S17). The fluctuation of FE_{NH_3} and Y_{NH_3}, which was obtained from UV-vis spectra with 1-h integrals, was relatively slight during the entire test cycle (Fig. 3h), which highlights the robust stability of CoO–Ru/CC for efficient NO_3^-RR. The structures of CoO and Ru can be clearly distinguished, as confirmed by TEM, HRTEM, and corresponding IFFT images after the NO_3^- reduction experiment (Fig. S18).

To increase our understanding of how each component in the CoO–Ru catalyst promotes NO_3^-RR, the values of potential (E) at $j = 5$ mA cm^{-2} taken from the LSV curves of the CoO–Ru/CC and CoO/CC catalysts in the $Na_2SO_4/NaNO_3$ or Na_2SO_4 electrolyte are collected in Fig. 4a. Notably, the E values of CoO–Ru/CC and CoO/CC in the $Na_2SO_4/NaNO_3$ electrolyte are lower than those in the Na_2SO_4 electrolyte, and particularly for the case of CoO–Ru/CC, the significance of the decrease is greater, which reveals that the introduction of metallic Ru is highly beneficial for the NO_3^-RR. Moreover, as derived from the Tafel curves of CoO–Ru/CC and CoO/CC in Na_2SO_4 electrolyte, the Tafel slope of CoO–Ru/CC (530 mV dec^{-1}) is higher than that of CoO/CC (326 mV dec^{-1}) (Fig. 4b), which indicates that Ru also can inhibit the occurrence of hydrogen evolution side reactions.[34]

To evaluate the intrinsic activity of the CoO–Ru/CC and CoO/CC catalysts, the electrochemically active surface area (ECSA) can be determined by the double layer capacitance (C_{dl}) measured from the cyclic voltammograms with a series of scan rates (10–50 mV s^{-1}) in the potential window that is free of faradaic process (Fig. S19). The C_{dl} of catalysts is the slope value of the linear fitting curve that is based on the double-layer capacitive currents Δj at 0.0 V *versus* open circuit potential (OCP) against scan rates. The C_{dl} value of CoO–Ru/CC is calculated as 495 μF cm^{-2}, which is higher than that of CoO/CC (435 μF cm^{-2}) (Fig. 4c), and accordingly, the ECSAs of CoO–Ru/CC and CoO/CC are 3.09 cm^2 and 2.72 cm^2, respectively. In addition, the partial current density for NH_3 production ($j$$NH_3$-ECSA) relative to the geometric area electrode is normalized to the ECSA, as shown in Fig. 4d. Evidently, CoO–Ru/CC delivers a higher $j$$NH_3$-ECSA than CoO/CC at different potentials, revealing that eutectic Ru enhances the intrinsic activity of CoO. The reaction rate order of NO_3^- reduction is reflected by the fitting slope of the logarithmic $|j|$ against the logarithmic NO_3^- concentration at different electrolysis potentials (Fig. 4e).[61] As shown in Fig. 4f, the rate order of NO_3^- reduction on CoO–Ru/CC is less than 1, which reveals that the capacity of CoO–Ru/CC to adsorb NO_3^- is stronger, and a higher coverage of NO_3^- is formed on the catalyst surface.

Electrochemical *in situ* Raman and ATR-FTIR techniques (Fig. S20 and S21) were conducted at the potential of −1.0 V (*vs.* RHE) to determine the specific intermediate and corresponding products over the NO_3^-RR. As recorded in the Raman spectra (Fig. 5a), the bands centered at 1045 and 1370 cm^{-1} are related to the vibrational modes of aqueous NO_3^- and adsorbed NO_3^- ($*NO_3$), respectively. As the NO_3^- reduction progresses, the peak intensity of $*NO_3^-$ decreases, while the bands, which are related to $*NH_3$ intermediates (1606 cm^{-1}), *NH intermediates (1506 cm^{-1}), and aqueous NH_3 (1122 cm−1), are continuously detected. In the ATR-FTIR spectra (Fig. 5b), the band at 1350 cm^{-1} was ascribed to the asymmetrical N–O stretching vibration of NO_3^- (ν-NO_3^-).[21] In the NO_3^-RR process, the

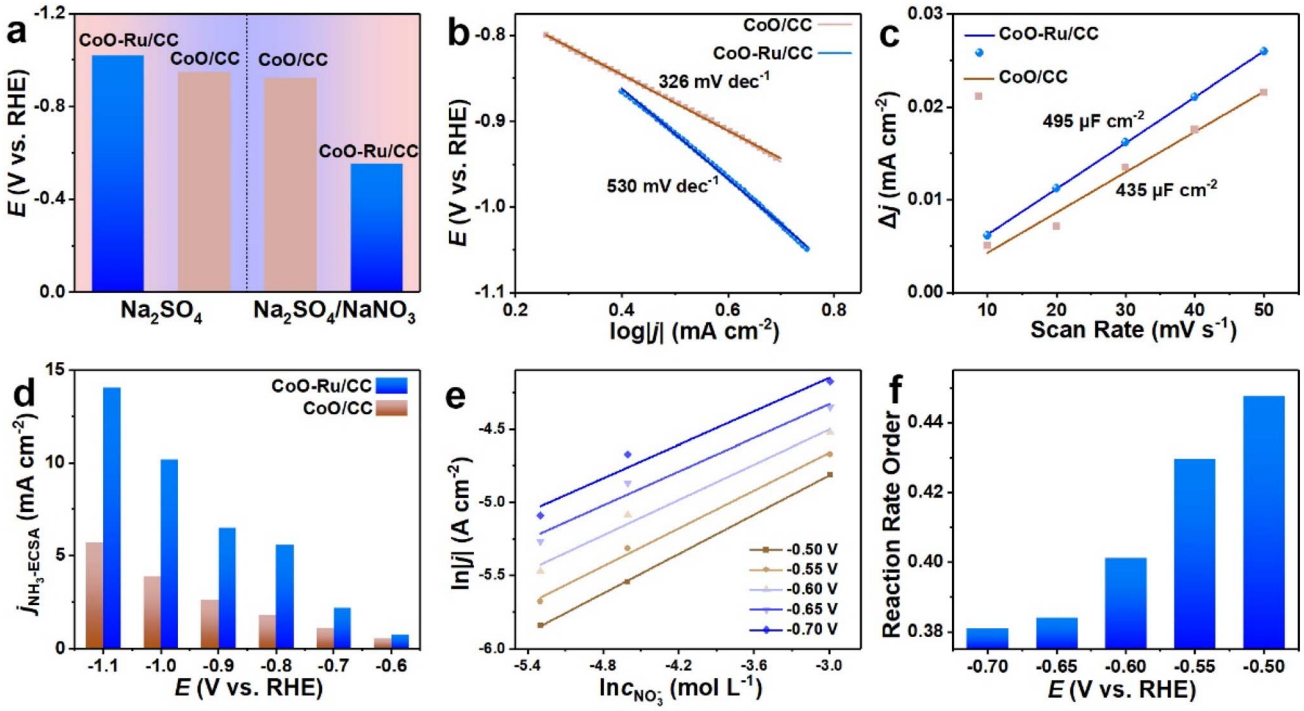

Fig. 4 (a) The values of E at a current density of 5 mA cm^{-2}. (b) Tafel curves for CoO–Ru/CC and CoO/CC in Na_2SO_4 electrolyte. (c) Linear fitting of the double-layer capacitive current Δj at 0.0 V *vs.* OCP against scan rate. (d) NH_3 partial current densities normalized to the ECSA. (e) Linear fitting of ln j against ln $c_{NO_3^-}$ of CoO–Ru/CC for NO_3^- reduction at various potentials. (f) The rate order of CoO–Ru/CC for NO_3^- reduction.

vibrational Stark effect was detected for bands between 1400 and 1350 cm^{-1}, revealing the breakage of N–O bonds.[28] The discernible band at 1124 cm^{-1}, corresponding to the stretching vibration of the N–O bond (ν-NO), reveals the key *NO intermediate in the product selection.[29] Additionally, the band at 1632 cm^{-1}, which was attributed to the N–H bending band (δ-NH), reveals that an *NH intermediate is generated.[31] Moreover, the characteristic peak of *NH_3 (ad-NH_3) and the N–H bond-bending vibration of the *NH_2 intermediate (ν-NH_2) appear at 1150 and 1448 cm^{-1}, respectively, demonstrating the successive deoxygenation and protonation processes of NO_3^-.[31] The band at approximately 1638 cm^{-1} was attributed to the O–H bond that is responsible for water splitting and generating *H involved in the hydrodeoxidation of NO_3^- in solution.[30]

To gain in-depth insights into the mechanism of the reaction of NO_3^-RR to NH_3, density functional theory (DFT) calculations were conducted in detail. The CoO–Ru structure (Fig. S22) was rationally created based on the characterization results described above. Bader charge analysis shows that a charge of approximately 0.024 e$^-$ per Ru atom was transferred to CoO (Fig. S23a) from the Ru (Fig. S23b) catalyst, which confirms the charge change induced by the interface interaction between the two. Considering that inhibiting H* coupling is very beneficial for promoting the process of NO_3^- reduction to NH_3, the Gibbs free energy change (ΔG) of H* coupling on the CoO, Ru, and CoO–Ru catalysts was investigated, as illustrated in Fig. 5c. In comparison with single-phase CoO or Ru, the ΔG of the H* coupling on CoO–Ru was larger when it originated from the exposed Ru atomic sites around the CoO–Ru interfacial structure, which indicates that the prepared CoO–Ru catalyst more easily performs hydrogenation in the NO_3^- reduction process. Additionally, the adsorption of catalysts for NO_3^- species determines whether the NO_3^-RR can smoothly proceed. Fig. 5d shows the ΔG of adsorption and the corresponding adsorption configurations of NO_3^- species on CoO–Ru (configurations 1–3) and CoO (configurations 4 and 5). Overall, the ΔG of NO_3^- species on CoO–Ru is negative, while it is positive on CoO, revealing that NO_3^- species are more likely to be adsorbed on the CoO–Ru catalyst. Fig. 5e illustrates the adsorption values of ΔG and the corresponding optimized adsorption configurations of the deoxidation hydrogenation process for NO_3^- species *via* the transfer of nine protons and eight electrons. Among the three adsorption configurations of NO_3^- species on CoO–Ru, the ΔG of configuration 3 (−0.98 eV) is the lowest, indicating that it is more advantageous for adsorption of NO_3^- species to occur with configuration 3. Two O atoms of NO_3^- species were adsorbed on two Ru atoms of CoO–Ru in configuration 3 (Fig. S24). Due to the activation of adsorbed NO_3^- species by exposed Ru atoms, the N–O bonds were elongated with lengths of 1.223 Å (N–O_1), 1.311 Å (N–O_2), and 1.314 Å (N–O_3). On the heels of adsorbing NO_3^- species, the *NO_3 intermediate was hydrogenated by the ($H^+ + e^-$) pair through two forms of *NO_3H and *NO_2–OH, in which it is energetically favorable for generating the *NO_2*OH intermediate (−1.31 eV), but unfavorable for the *NO_3H intermediate (0.46 eV). The underlying reason for this is the fact that the N–O_3 bond in the *NO_3 intermediate

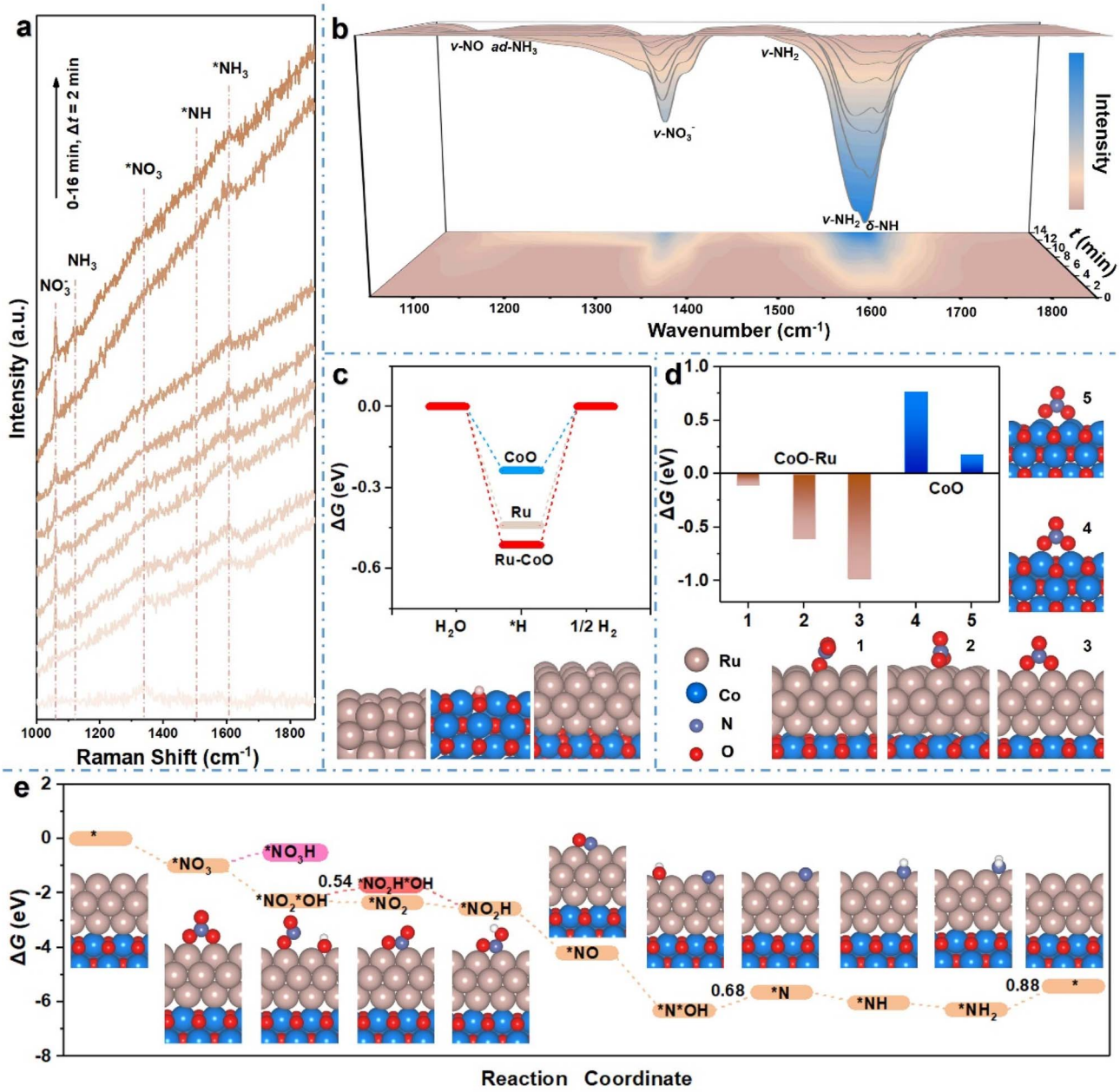

Fig. 5 *In-situ* (a) Raman and (b) ATR-FTIR spectra of CoO–Ru as a function of reaction time at −1.0 V *vs.* RHE. (c) Δ*G* for the coupling of H* on the corresponding optimized CoO, Ru, and CoO–Ru configurations. (d) ΔG_{ad} and the corresponding adsorption configurations of NO_3^- species on CoO and CoO–Ru surfaces. (e) Δ*G* of reaction intermediates for the process of NO_3^- reduction to NH_3 on CoO–Ru and the corresponding optimized configurations of series of intermediates. Ru, Co, N and O atoms are shown in pale brown, blue, grayish blue and red, respectively.

activated by the exposed Ru atoms is more inclined to break after stretching, and the shed O atom is adsorbed on the nearby Ru atom catalyst for hydrogenation. Thus, in the following step, hydrogenation can proceed by the desorption of H_2O to obtain a nitrite intermediate (*NO_2) or the formation of the *NO_2H–OH intermediate. By comparing the values of Δ*G*, it is revealed that the desorption of H_2O is a downhill step (−0.06 eV), while the formation of *NO_2H–OH is a slight uphill step ($\Delta G = 0.54$ eV). Subsequently, the Δ*G* of these processes (*NO_2 → *NO_2H → *NO) continuously decreases. It is worthwhile to note that the N–O bond in the *NO intermediate will break in the subsequent hydrogenation step to form the *N*OH intermediate. Obviously, the N–O bonds of NO_3^- species adsorbed on the CoO–Ru catalyst are easily dissociated during the continuous hydrogenation processes, which can reduce the selectivity of nitrite (NO_2^-). The subsequent hydrogenation to the dehydration process (*N*OH → *N) is an uphill step, with a Δ*G* of 0.68 eV. The remaining step is the continuous hydrogenation of *N to produce NH_3, and the rate-determining step (RDS) is the desorption of NH_3 with a high barrier of 0.88 eV, due to the

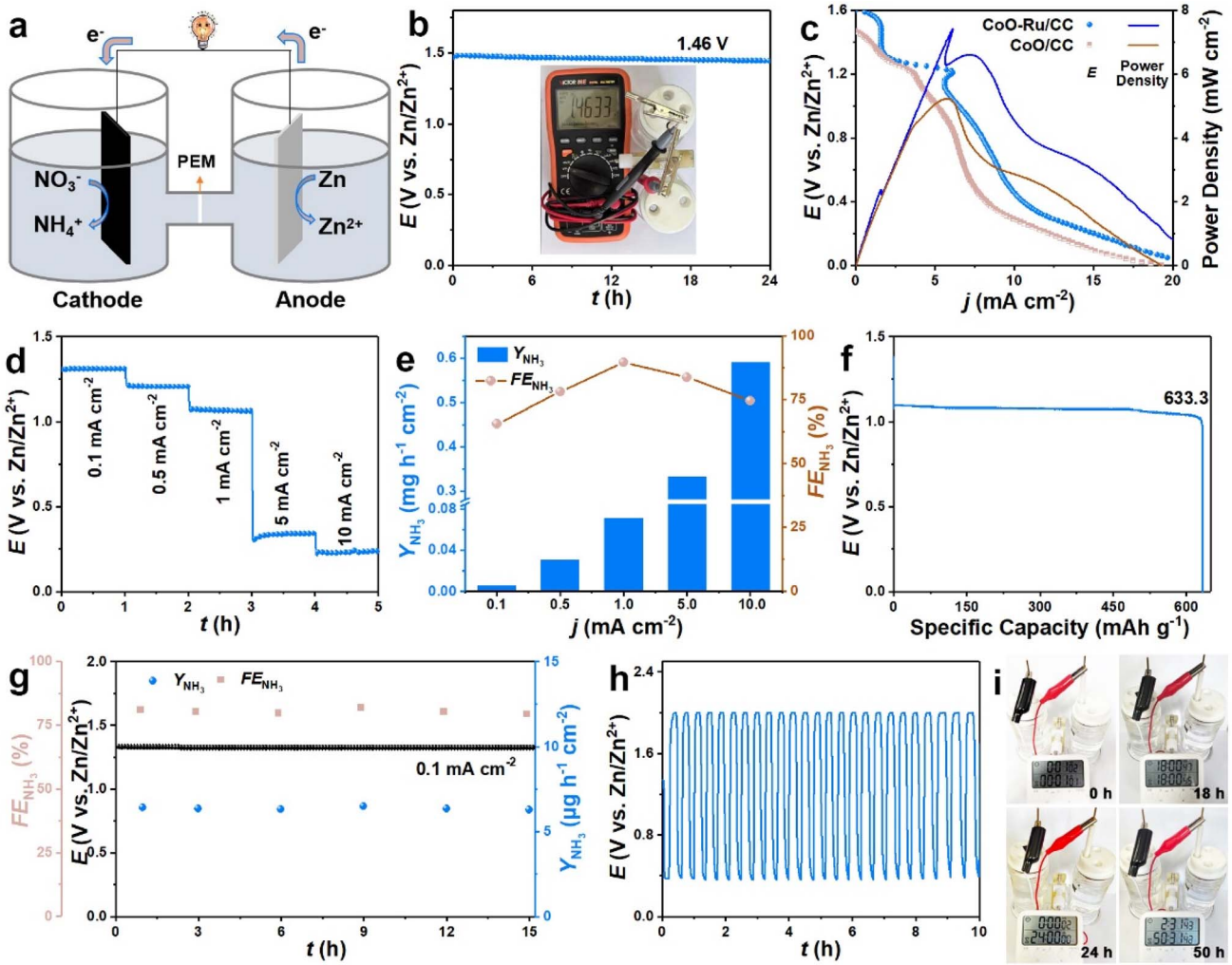

Fig. 6 (a) A schematic illustration of an assembled Zn–NO_3^- battery with a Zn anode and CoO–Ru/CC cathode. (b) The OCP of the CoO–Ru/CC-based Zn–NO_3^- battery. (c) Discharge curves and the corresponding power density. (d) Discharge tests at a series of current densities and (e) the corresponding Y_{NH_3} and FE_{NH_3} values. (f) Specific capacity for the CoO–Ru/CC-based Zn–NO_3^- battery at a current density of 1 mA cm^{-2}. (g) Long-term discharge testing and the corresponding Y_{NH_3} and FE_{NH_3} values. (h) Discharge–charge processes at a constant current density of 1 mA cm^{-2}. (i) Digital photos showing the powering of a commercial electronic timer by a set of CoO–Ru/CC-based Zn–NO_3^- batteries.

strong adsorption of N on the Ru–Ru site. It is therefore easy to conclude that the key $*NO_2$, *NO, *N, and *NH intermediates follow the NO_3^-RR pathway, which can be referred to as the $*NO_3$–$*NO_2$–*NO–*N–*NH–$*NH_2$–$*NH_3$ pathway for our CoO–Ru catalyst.

3.3. Electrochemical evaluation of Zn–NO_3^- batteries

Based on the excellent catalytic activity and selectivity of CoO–Ru/CC for the eight-electron process of NO_3^- reduction to NH_3 production, a novel rechargeable Zn–NO_3^- battery device was assembled. As schematically depicted in Fig. 6a, the configuration of the Zn–NO_3^- device includes CoO–Ru/CC (or CoO/CC) as the cathode, and Zn foil as the anode. The CoO–Ru/CC-based Zn–NO_3^- battery provides an OCP of 1.46 V (*vs.* Zn/Zn^{2+}), as shown in Fig. 6b, which is higher than that of a CoO/CC-based Zn–NO_3^- cell (1.38 V, Fig. S25). In addition, the stability of the OCP was maintained for up to 24 h, which reveals the considerable ability of CoO–Ru/CC-based cells to sustain a constant voltage over an extended period. Discharge potentiodynamic measurements for CoO–Ru/CC- and CoO/CC-based Zn–NO_3^- batteries were conducted, and the corresponding power density was calculated. As profiled in Fig. 6c, the polarization curves are mainly divided into two parts: OCP > E > 0.4 V and 0.4 V > E > 0 V (*vs.* Zn/Zn^{2+}). The relatively large potential offset range (OCP > E > 0.4 V) may be related to the adsorption of NO_3^-.[62] Moreover, there is a decrease in j at 1.2 V (*vs.* Zn/Zn^{2+}) for the polarization curve of the CoO–Ru/CC-based Zn–NO_3^- battery, which was possibly attributed to the rapid adsorption of NO_3^- in CoO–Ru/CC, which subsequently formed an adsorption layer. The discharge power density of the CoO–Ru/CC-based battery is 7.41 mW cm^{-2} at 1.21 V (*vs.* Zn/Zn^{2+}), which is higher than that of CoO/CC (5.26 mW cm^{-2} at 0.90 V *vs.* Zn/Zn^{2+}). The power density may be affected by internal resistance and ionic conductivity, which can be demonstrated by

electrochemical impedance spectroscopy (EIS) (Fig. S26). From the Nyquist plots, CoO–Ru/CC and CoO/CC produced a semicircle in the high-medium frequency region, and an inclined line at the low frequency range. A smaller *x*-intercept in the high frequency region and steeper slope in the low frequency range was obtained for CoO–Ru/CC, which indicates lower internal resistance and high ionic conductivity. In addition, the discharge power density was also influenced by cathode wettability, which was proved through contact angle measurement (Fig. S27). CoO–Ru/CC shows a contact angle of approximately 27.8°, which is smaller than that of CoO–Ru/CC (39.01°), revealing the increased wettability of CoO–Ru/CC. At a series of discharge current densities from 0.1 to 10 mA cm^{-2}, the CoO–To verify the performance of the CoO–Ru/CC-based Zn–NO_3^- battery exhibited a stable discharge curve, indicating its excellent rate performance along with a modest voltage drop with increasing current density (Fig. 6d). To verify the performance of the CoO–Ru/CC-based Zn–NO_3^- battery for producing NH_3, the amount of NH_3 in the cathode chamber was measured after discharged for 1 h at various discharge current densities (Fig. S26). It should be noted that the Zn–NO_3^- battery can simultaneously output electrical energy and reduce NO_3^- to NH_3. Fig. 6e presents the calculated Y_{HN_3} and FE_{HN_3}, in which the maximum FE_{HN_3} is 89.60% at j = 1.0 mA cm^{-2}, and the highest Y_{HN_3} is 0.59 mg h^{-1} $cm_{cat.}^{-2}$ at j = 10 mA cm^{-2}. At a current density of 1 mA cm^{-2}, the CoO–Ru/CC-based Zn–NO_3^- battery delivered a specific capacity as high as 633.3 mAh g^{-1} (Fig. 6f), corresponding to a high energy density of 682.6 mWh g^{-1}, transcending other previous reports (Co–B@CoO_x: 677.7 mWh g^{-1}; o-CoP/C@Cu_3P/CF: 282.9 mWh g^{-1}).[63,64] A 15-h long-term discharging test was carried out at a current density of 0.1 mA cm^{-2}. The corresponding discharge potential remained at 1.33 V (*vs.* Zn/Zn^{2+}), and the fluctuations of calculated Y_{HN_3} and FE_{HN_3} at time-series points were small (Fig. 6g and Fig. S27), revealing that the CoO–Ru/CC-based Zn–NO_3^- battery possessed long-term stability for efficient NH_3 production and supplying electricity. The CoO–Ru/CC-based Zn-NO_3^- battery also showed no obvious change in the charge–discharge potential gap after a 10-h cycling test (Fig. 6h). Remarkably, two CoO–Ru/CC-based Zn–NO_3^- batteries connected in series were able to successfully illuminate a red light-emitting diode (LED) (Fig. S28). More impressively, a set of CoO–Ru/CC-based Zn–NO_3^- batteries successfully powered a commercial electronic timer (powered by a 1.5 V dry battery) for over 50 h (Fig. 6i). All the above results explicitly prove that there are enormous commercial applications for CoO–Ru/CC as a cathode for a Zn–NO_3^- battery in energy supply and conversion from NO_3^- to NH_3.

4. Conclusions

Herein, we devised a facile yet efficient strategy to fabricate the hetero hybrid electrocatalyst of CoO–Ru/CC, which uniformly anchored pre-reduced nano-dimensional Ru on NNs assembled into hierarchical CoO microspheres that were self-supported upon 3D porous CC. The self-standing porous NNs assembled into a hierarchical CoO–Ru micro-spherical framework were endowed with abundant active three-phase sur-/interfaces and oxygen vacancies, which optimized the adsorption of NO_3^- and favored the breakage of N–O bonds. Moreover, the CoO–Ru NNs induced a local electric field, which adequately retained reaction intermediates (*i.e.*, $*NO_2$, *NO, *N, and *H species), improving the selectivity of NH_3 rather than H_2 by-production and also reducing the reaction energy barrier. Benefiting from the appealing merits of nanostructure and composition, CoO–Ru/CC showed a high faradaic efficiency of 93.41%, and an NH_3 yield rate of 2.502 mg h^{-1} cm^{-2} at −1.0 V (*vs.* RHE). Additionally, the CoO–Ru/CC-based Zn–NO_3^- battery exhibited a power density of 7.41 mW cm^{-2} and a high NH_3 faradaic efficiency of 89.60%. The $*NO_3$–$*NO_2$–*NO–*N–*NH–$*NH_2$–$*NH_3$ pathway involves an electrocatalytic reduction mechanism that was reasonably put forward for CoO–Ru/CC as well, as evidenced by the detailed *in(ex)-situ* physicochemical characteristics and DFT calculations. More essentially, our work provides important directive significance for the rational design of next-generation electrocatalysts for efficient eRNO_3^--to-NH_3 conversion in the future.

Author contributions

Jinxiu Zhao: conceptualization, data curation, formal analysis, funding acquisition, investigation, methodology, project administration, writing–original draft. Xuejing Liu: formal analysis, methodology, software, writing–review and editing. Xiang Ren: formal analysis, funding acquisition, writing–review and editing. Dan Zhao: conceptualization, data curation, writing–review and editing. Zhen Li: software, writing–review and editing. Qing Kang: software, writing–review and editing. Xuewen Zhang: software, writing–review and editing. Linrui Hou: funding acquisition, writing–review and editing. Qin Wei: funding acquisition, writing–review and editing. Changzhou Yuan: funding acquisition, writing–review and editing.

Conflicts of interest

There are no conflicts to declare.

Data availability

All relevant data are within the main article and its supplementary information (SI). Supplementary information: XPS, UPS, TEM, HRTEM, EDX, LSV, CV. See DOI: https://doi.org/10.1039/d5sc09240j.

Acknowledgements

The authors acknowledge the financial support from the National Natural Science Foundation of China (No. U22A20145, 52171211, 52271218, 52572228), the Major Program of Shandong Province Natural Science Foundation (No. ZR2023ZD43), and the Natural Science Foundation of Shandong Province (No. ZR2024QB042, ZR2025MS717).

References

1 H. Ishaq and C. Crawford, *Energy Convers. Manage.*, 2024, **300**, 117869.
2 P. Lan, S. Chen, Q. Li, K. Li, F. Wang, Y. Zhao and T. Wang, *Renew. Energy*, 2024, **227**, 120602.
3 G. Leigh, in *Catalysts for Nitrogen Fixation*, Springer, Berlin, Heidelberg 2004, pp. 33–54.
4 H. Xu, Y. Ma, J. Chen, W. Zhang and J. Yang, *Chem. Soc. Rev.*, 2022, **51**, 2710–2758.
5 C. Smith and L. Torrente-Murciano, *Nat. Chem. Eng.*, 2025, **2**, 261–272.
6 A. E. Shilov, *Russ. Chem. Bull.*, 2003, **52**, 2555–2562.
7 A. Stirling, I. Pápai, J. Mink and D. R. Salahub, *J. Chem. Phys.*, 1994, **100**, 2910–2923.
8 E. Abascal, L. Gómez-Coma, I. Ortiz and A. Ortiz, *Sci. Total Environ.*, 2022, **810**, 152233.
9 D. Liu, L. Qiao, S. Peng, H. Bai, C. Liu, W. F. Ip, K. H. Lo, H. Liu, K. W. Ng, S. Wang, X. Yang and H. Pan, *Adv. Funct. Mater.*, 2023, **33**, 2303480.
10 Y. Xiong, Y. Wang, J. Zhou, F. Liu, F. Hao and Z. Fan, *Adv. Mater.*, 2024, **36**, 2304021.
11 X. Liang, H. Zhu, X. Yang, S. Xue, Z. Liang, X. Ren, A. Liu and G. Wu, *Small Methods*, 2023, **4**, 2200202.
12 W. Zhong, Z. Gong, P. Chen, Q. Cao, X. Liu, Y. Chen and Z. Lin, *Chem Catal.*, 2024, **4**, 101060.
13 V. T. Chebrolu, D. Jang, G. M. Rani, C. Lim, K. Yong and W. B. Kim, *Carbon Energy*, 2023, **5**, e361.
14 W. Wen, S. Fang, Y. Zhou, Y. Zhao, P. Li and X. Yu, *Angew. Chem., Int. Ed.*, 2024, **63**, e202408382.
15 P. Li, R. Li, Y. Liu, M. Xie, Z. Jin and G. Yu, *J. Am. Chem. Soc.*, 2023, **145**, 6471–6479.
16 Y. Huang, C. He, C. Cheng, S. Han, M. He, Y. Wang, N. Meng, B. Zhang, Q. Lu and Y. Yu, *Nat. Commun.*, 2023, **14**, 7368.
17 W. Zhong, Q. Hong, Q. Du, B. Y. Xia, X. Ai, F. Li and Y. Chen, *Energy Environ. Sci.*, 2025, **18**, 4971–4981.
18 S. Sarkar, A. Adalder, S. Paul, S. Kapse, R. Thapa and U. K. Ghorai, *Appl. Catal., B*, 2024, **343**, 123580.
19 S. Bhowmick, A. Adalder, A. Maiti, S. Kapse, R. Thapa, S. Mondald and U. K. Ghorai, *Chem. Sci.*, 2025, **16**, 4806–4814.
20 A. Adalder, S. Paul, N. Barman, A. Bera, S. Sarkar, N. Mukherjee, R. Thapa and U. K. Ghorai, *ACS Catal.*, 2023, **13**, 13516–13527.
21 J. Fang, Q. Zheng, Y. Lou, K. Zhao, S. Hu, G. Li, O. Akdim, X. Huang and S. Sun, *Nat. Commun.*, 2022, **13**, 7899.
22 L. Fang, S. Wang, S. Lu, F. Yin, Y. Dai, L. Chang and H. Liu, *Chin. Chem. Lett.*, 2024, **35**, 108864.
23 L. Dai, S. Li, Y. Dai, Y. Zheng, K. Liu, H. Li and B. Jiang, *Chem. Eng. J.*, 2024, **498**, 155735.
24 Y. Sun, Y. Shi, Y. Gao, M. Sun, Y. Yao, H. Yu, Y. Xu c, X. Wang and Y. Yang, *Chem. Eng. J.*, 2025, **512**, 162506.
25 J. Liu, Y. Li, X. Jia, J. Shen, Y. Zhu and C. Li, *Small*, 2025, **21**, 2408279.
26 Y.-Z. Yu, Y. Cheng, S. Cheng and Z.-Y. Wu, *Adv. Mater.*, 2025, **37**, 2412363.
27 J. Su, K. Shi, B. Liu, Z. Xi, J. Yu, X. Xu, P. Jing, R. Gao and J. Zhang, *Adv. Funct. Mater.*, 2024, **34**, 2401194.
28 N. C. Kani, N. H. L. Nguyen, K. Markel, R. R. Bhawnani, B. Shindel, K. Sharma, S. Kim, V. P. Dravid, V. Berry, J. A. Gauthier and M. R. Singh, *Adv. Energy Mater.*, 2023, **13**, 2204236.
29 J. Zhou, M. Wen, R. Huang, Q. Wu, Y. Luo, Y. Tian, G. Wei and Y. Fu, *Energy Environ. Sci.*, 2023, **16**, 2611–2620.
30 X. Zhang, X. Liu, Z. Huang, L. Gan, S. Zhang, R. Jia, M. Ajmal, L. Pan, C. Shi, X. Zhang, G. Yang and J. Zou, *Energy Environ. Sci.*, 2024, **17**, 6717–6727.
31 Y. Ren, C. Yu, L. Wang, L. Wang, X. Tan, Z. Wang, Q. Wei, Y. Zhang and J. Qiu, *J. Am. Chem. Soc.*, 2022, **144**, 10193–10200.
32 F. Chen, Z. Wu, S. Gupta, D. J. Rivera, S. V. Lambeets, S. Pecaut, J. Y. T. Kim, P. Zhu, Y. Z. Finfrock, D. M. Meira, G. King, G. Gao, W. Xu, D. A. Cullen, H. Zhou, Y. Han, D. E. Perea, C. L. Muhich and H. Wang, *Nat. Nanotechnol.*, 2022, **17**, 759–767.
33 Y. Wang, A. Xu, Z. Wang, L. Huang, J. Li, F. Li, J. Wicks, M. Luo, D. Nam, C.-S. Tan, Y. Ding, J. Wu, Y. Lum, C. Dinh, D. Sinton, G. Zheng and E. H. Sargent, *J. Am. Chem. Soc.*, 2020, **142**, 5702–5708.
34 L. Wu, J. Feng, L. Zhang, S. Jia, X. Song, Q. Zhu, X. Kang, X. Xing, X. Sun and B. Han, *Angew. Chem., Int. Ed.*, 2023, **62**, e202307952.
35 K. Fan, W. Xie, J. Li, Y. Sun, P. Xu, Y. Tang, Z. Li and M. Shao, *Nat. Commun.*, 2022, **13**, 7958.
36 Y. Zhou, R. Duan, H. Li, M. Zhao, C. Ding and C. Li, *ACS Catal.*, 2023, **13**, 10846–10854.
37 J. Zhou, M. Wen, R. Huang, Q. Wu, Y. Luo, Y. Tian, G. Wei and Y. Fu, *Energy Environ. Sci.*, 2023, **16**, 2611–2620.
38 X. Zhang, X. Liu, Z. Huang, L. Gan, S. Zhang, R. Jia, M. Ajmal, L. Pan, C. Shi, X. Zhang, G. Yang and J. Zou, *Energy Environ. Sci.*, 2024, **17**, 6717–6727.
39 Y. Guo, R. Zhang, S. Zhang, Y. Zhao, Q. Yang, Z. Huang, B. Dong and C. Zhi, *Energy Environ. Sci.*, 2021, **14**, 3938–3944.
40 X. Xu, X. Liu, J. Zhao, D. Wu, Y. Du, T. Yan, N. Zhang, X. Ren and Q. Wei, *J. Colloid Interface Sci.*, 2022, **606**, 1374–1380.
41 D. Zhu, L. Zhang, R. E. Ruther and R. J. Hamers, *Nat. Mater.*, 2013, **12**, 836–841.
42 G. Kresse and J. Furthmuller, *Phys. Rev. B:Condens. Matter Mater. Phys.*, 1996, **54**, 11169–11186.
43 P. E. Blöchl, *Phys. Rev. B:Condens. Matter Mater. Phys.*, 1994, **50**, 17953–17979.
44 J. P. Perdew, K. Burke and M. Ernzerhof, *Phys. Rev. Lett.*, 1996, **77**, 3865–3868.
45 M. J. Redman and E. G. Steward, *Nature*, 1962, **193**, 867.
46 V. Wang, N. Xu, J. C. Liu, G. Tang and W. T. Geng, *Comput. Phys. Commun.*, 2021, **267**, 108033.
47 K. Momma and F. Izuma, *J. Appl. Crystallogr.*, 2011, **44**, 1272–1276.
48 J. K. Nørskov, J. Rossmeisl, A. Logadottir, L. Lindqvist, J. R. Kitchin, T. Bligaard and H. Jonsson, *J. Phys. Chem. B*, 2004, **108**, 17886–17892.
49 J. Liu, D. Richards, N. Singh and B. R. Goldsmith, *ACS Catal.*, 2019, **9**, 7052–7064.

50 F. Han, G. Li, Y. Liu, A. Wang, F. Wang, T. Zhang and N. Li, *Green Chem.*, 2024, **26**, 936–947.
51 M. Zhao, L. Figueroa-Cosme, A. O. Elnabawy, M. Vara, X. Yang, L. T. Roling, M. Chi, M. Mavrikakis and Y. Xia, *Nano Lett.*, 2016, **16**, 5310–5317.
52 H. Liu, J. Sun, Z. Xu, W. Zhou, C. Han, G. Yang and Y. Shan, *J. Electroanal. Chem.*, 2022, **911**, 116213.
53 J. A. Parambil, V. M. Abdul Mujeeb, K. P. Sreenivasan and P. Jayaram, *J. Sol-Gel Sci. Technol.*, 2021, **98**, 452–461.
54 Y. Wang, X. Xu, Y. Wu, F. Li, W. Fan, Y. Wu, S. Ji, J. Zhao, J. Liu and Y. Huo, *Adv. Energy Mater.*, 2024, **14**, 2401833.
55 H. Wu, Y. Cui, G. Gao, Y. Wang and J. Li, *J. Alloys Compd.*, 2023, **960**, 170847.
56 Y. Li, L. Wang, F. Zhang, W. Zhang, G. Shao and P. Zhang, *Adv. Sci.*, 2023, **10**, 2205020.
57 K. Chen, T. Jiang, T. Liu, J. Yu, S. Zhou, A. Ali, S. Wang, Y. Liu, L. Zhu and X. Xu, *Adv. Funct. Mater.*, 2022, **32**, 2109366.
58 R. Jia, Y. Wang, C. Wang, Y. Ling, Y. Yu and B. Zhang, *ACS Catal.*, 2020, **10**, 3533–3540.
59 Z. Pu, Q. Liu, C. Chen and F. Wang, *Chem. Eng. J.*, 2024, **497**, 154861.
60 N. Mukherjee, A. Adalder, S. Paul, N. Barman, R. Thapa, K. Mitra, R. Urkude and U. K. Ghorai, *Adv. Funct. Mater.*, 2025, **35**, e19797.
61 Z. Chen, Y. Zhao, H. Huang, G. Liu, H. Zhang, Y. Yan, H. Li, L. Liu, M. Liu, D. Wang and J. Zeng, *J. Am. Chem. Soc.*, 2025, **147**, 18737–18746.
62 J. Lu, S. Lv, H. S. Park and Q. Chen, *J. Hazard. Mater.*, 2024, **477**, 135287.
63 X. Zhu, C. Ma, Y. Wang, K. Qu, L. Song, J. Wang, Y. Gong, X. Liu, J. Zhang, Q. Lu and A. Wang, *Energy Environ. Sci.*, 2024, **17**, 2908–2920.
64 Y. Li, Z. Lu, L. Zheng, X. Yan, J. Xie, Z. Yu, S. Zhang, F. Jiang and H. Chen, *Energy Environ. Sci.*, 2024, **17**, 4582–4593.